ELSEVIER

Journal of Fluids and Structures 21 (2005) 561–577

JOURNAL OF FLUIDS AND STRUCTURES

www.elsevier.com/locate/jfs

A new tube/support impact model for heat exchanger tubes

M.A. Hassan[a,*], D.S. Weaver[b], M.A. Dokainish[b]

[a]*Mechanical Engineering Department, University of New Brunswick, Fredericton, Canada E3B 5A3*
[b]*Department of Mechanical Engineering, McMaster University, Hamilton, Ont., Canada L8S 4L7*

Received 10 January 2005; accepted 31 July 2005
Available online 21 October 2005

Abstract

Heat exchanger tubes are often loosely supported at intermediate points by plates or flat bars. Flow-induced vibrations result in fretting wear tube damage due to impacting and rubbing of tubes against their supports. Prediction of tube response relies on modelling the nonlinear tube/support interaction. The evaluated response is used to predict the resultant wear damage using experimentally measured wear coefficients. An accurate prediction of impact forces and work rate is therefore paramount. The analytical models available in the open literature generally assume tube/support contact occurs at a single point. In this paper, a computational algorithm is proposed to describe tube/support impact considering a finite support width. The new model provides a means of representing tube/support contact as a combination of edge and segmental contact. The proposed model utilizes a distributed contact stiffness to describe the segmental contact. The formulation also incorporates a stick/slip friction model. The model developed is utilized to simulate the dynamics of loosely supported tubes.

Keywords: Impact; Heat exchangers; Finite elements method; Nonlinear dynamics

1. Introduction

Many industries, such as process and power plants, utilize high thermal efficiency shell and tube heat exchanger designs. Performance requirements often dictate high coolant velocities and flexible tubes, which in turn may cause tubes to experience excessive flow-induced vibrations. A great deal of research has been devoted to flow-induced vibrations due to their practical significance (Païdoussis, 1982; Chen, 1991; Weaver et al., 2000; Pettigrew and Taylor, 2003). These research efforts have led to many improvements in understanding the mechanisms of flow-induced vibrations.

Parameters that affect tube wear can be measured during wear tests. In practical cases, however, analytical techniques are necessary to estimate these effects from flow and vibration information. These techniques mainly utilize the nonlinear time-domain simulation of tube dynamics via the finite element method. This includes modelling the tube/support contact and friction forces. Modelling contact, in general, is a complex task due to the unknown contact interface and friction conditions. The solution of such problems involves complex searching algorithms and iterative procedures. However, such a general approach is not feasible in a flow-induced vibrations study in which large time

*Corresponding author.
E-mail address: hassanm@unb.ca (M.A. Hassan).

0889-9746/$ - see front matter © 2005 Elsevier Ltd. All rights reserved.
doi:10.1016/j.jfluidstructs.2005.07.016

records are required to obtain meaningful response average parameters. In such cases, the nonlinearity is localized and the contact region is reasonably defined. Based on this fact, several codes, such as VIBIC (Rogers and Pick, 1977; Fisher et al., 1989), H3DMAP (Sauvé and Teper, 1987; Morandin and Sauvé, 1999), GERBOISE (Axisa et al., 1988) and INDAP (Hassan et al., 2002, 2003) have been developed to simulate tube/support interaction. These codes have been utilized in the analysis of multispan tubes under simulated fluid forces and have yielded reasonable response and impact force results. The tube/support interaction models available in the open literature generally treat impact by introducing a spring at the support node. This greatly simplifies the modelling and results in a very efficient algorithm. Therefore, the support node is the only node that has to be monitored. In other words, the support is assumed to be a knife-edge type of support. However, in reality the support has a finite width which may not be well simulated using the traditional model because this model permits the tube to overlap with the support along the support width, as long as the contact node is within the support space. In addition, it is not possible to investigate the local distribution of contact pressure or the effect of the support width on tube dynamics and wear. Most of the published models make these kinds of assumptions. One approach to overcome this deficiency is to perform tube/support interaction computations by defining complex finite-length support geometries in terms of several contact locations along the support width. The single-point impact algorithm must be applied at each support a number of times (equal to the number of contact nodes per support). In addition, in the presence of significant axial motion (for example, in-plane motion in a U-bend tube) the algorithm may fail to handle some of the designated contact nodes being moved out of the support space.

This paper addresses the above shortcomings of the traditional formulations. This is accomplished by introducing an enhanced tube/support interaction model which recognises the effect of the support width. A brief review of the development of this model and its appropriateness is presented. For the most part, this paper is restricted to analysing lattice-bar supports. However, the same model can be applied to any other support types.

2. New tube/support contact model

There are several classifications of tube motion within a heat exchanger. Tube motion may be classified as impact, sliding, or combined impact and sliding (Ko, 1985; Kim et al., 1988). The existence of any of these motion types depends on the support geometry, the excitation level and the tube-to-support clearance. For example, when the preload is large enough to prevent tube/support separation, tube motion is basically the classical sliding type. On the other hand, when the clearance is large with a small preload, intermittent contact occurs. The tube/support contact configuration may change with the heat exchanger operating conditions. Tube/support interaction may also be categorized based on the type of contact. This is illustrated in Fig. 1 and includes two main types

(i) tube/support contact at the support edge (point contact);
(ii) tube/support contact over a line (segment contact).

The tube/support contact configuration may be a combination of the afore-mentioned components. The contribution of each of these components depends on the preload, support alignment, and tube-to-support radial clearance. Another classification categorizes the tube motion at the support location as rocking motion (point contact), and tube vibration with anti-nodes at the supports [segment contact (Kim et al., 1988)].

Traditionally, tube/support contact is modelled by introducing an equivalent contact stiffness at the support node. In such a model, the displacement of the contact node is monitored and impact takes place when the normal component of the displacements exceeds the radial clearance. As a result, if the radial clearance is small, the support provides a knife-edge type of support (Fig. 2). This model will be referred to herein as a single-point contact model (SPCM).

In the current work an attempt is made to model the tube/support contact in more accurate detail. In this section, the new formulation of the two contact configurations (edge and segment contact) will be presented separately. Within the finite element solution, however, they have been computed simultaneously.

2.1. Edge contact model

A generalized edge contact model is developed to model the situation in which the tube contacts the support at the edge (point contact). This situation is shown in Fig. 3 and is characterized by an overlap between the line connecting the principal contact node (PCN) (A), the neighbouring contact node (NCN) (E), and the support. This type of contact cannot be detected or modelled using the SPCM since the PCN (A) lies within the support clearance.

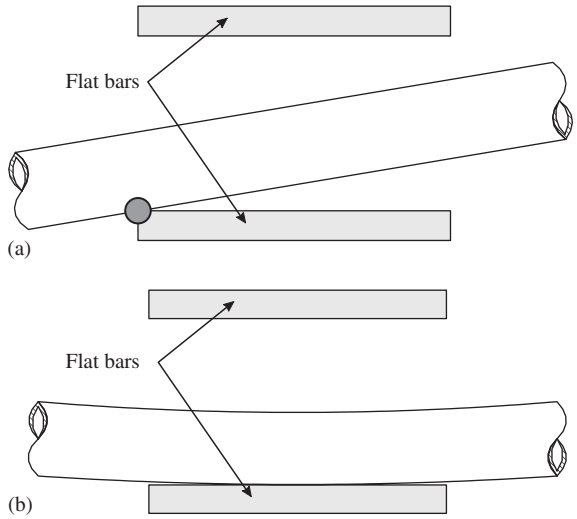

Fig. 1. Types of tube/support contact: (a) point contact and (b) segment contact.

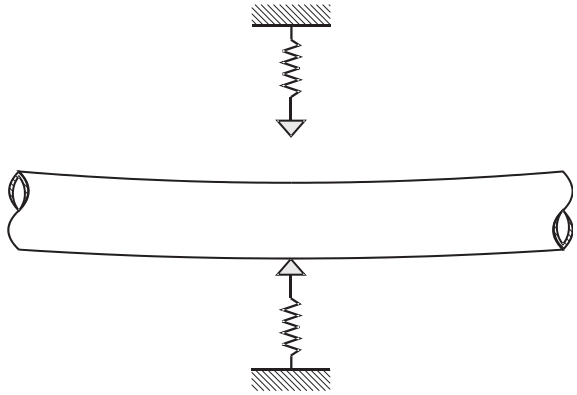

Fig. 2. Single-point contact (traditional) model.

The tube's axial unit vector is calculated according to the current configuration, such that

$$\widehat{u}_{ta} = \left[\frac{r_x^E - r_x^A}{L_e}\right]\widehat{e}_x + \left[\frac{r_y^E - r_y^A}{L_e}\right]\widehat{e}_y + \left[\frac{r_z^E - r_z^A}{L_e}\right]\widehat{e}_z, \tag{1}$$

where r_x, r_y, and r_z are position components with respect to the global coordinate system. L_e represents the element length and is given by

$$L_e = \left[(r_x^E - r_x^A)^2 + (r_y^E - r_y^A)^2 + (r_z^E - r_z^A)^2\right]^{1/2}. \tag{2}$$

Superscripts A and E refer to the current location of the PCN and the NCN, respectively. The tube's tangential ($\widehat{u}_{tt}$) and normal ($\widehat{u}_{tn}$) unit vectors are obtained by

$$\begin{aligned} \widehat{u}_{tt} &= \widehat{u}_{ta} \times \widehat{u}_{smn}, \\ \widehat{u}_{tn} &= \widehat{u}_{tt} \times \widehat{u}_{ta}, \end{aligned} \tag{3}$$

where $\widehat{u}_{smn}$ is the tube axial and support normal unit vectors (Fig. 4). Vectors pointing to the original positions of the PCN and the NCN are designated $\vec{A}_o$ and $\vec{E}_o$, respectively. At any instant of time (t), the current position of the PNC

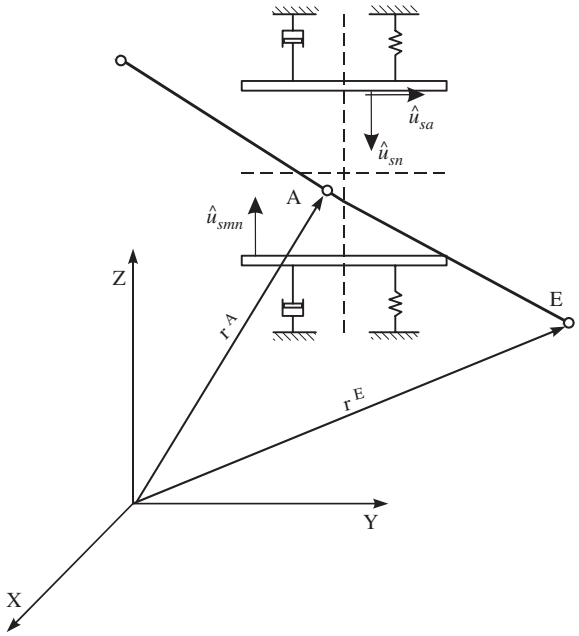

Fig. 3. Contact node set: principal contact node (A) and neighbouring contact nodes (E).

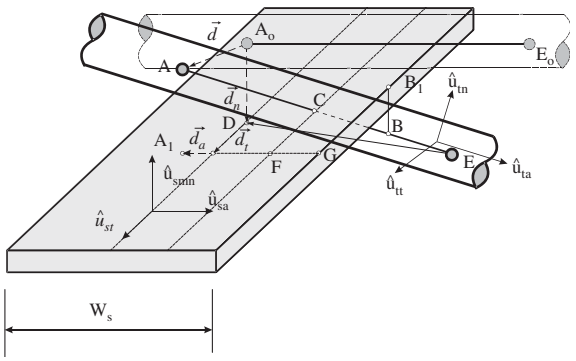

Fig. 4. Tube/support overlap geometry in case of edge contact.

and NCN are given by

$$\vec{A} = \vec{A}_o + \overrightarrow{d^A},$$
$$\vec{E} = \vec{E}_o + \overrightarrow{d^E}, \tag{4}$$

where $\overrightarrow{d^A}$ and $\overrightarrow{d^E}$ are the displacement vectors of the PCN and NCN, respectively. Both of these displacements have components in the directions of the support unit vectors. These components are the axial (d_a), the normal (d_n), and the tangential (d_t), and can be obtained by the dot-product of the displacement vector ($\vec{d}$) and the support unit vectors as follows:

$$d_a = \vec{d} \cdot \hat{u}_{sa},$$
$$d_n = \vec{d} \cdot \hat{u}_{smn},$$
$$d_t = \vec{d} \cdot \hat{u}_{st}. \tag{5}$$

Now, for inter-nodal point contact to occur, three conditions have to be fulfilled: (i) there must be no overlap between the principal contact node and the support; (ii) the normal component of the NCN has to be negative; and (iii) the point of intersection between the tube's outer surface and the support surface must be located within the support width.

Point B refers to the normal projection of the support edge on the tube's surface. The displacement at point B is obtained by using the beam interpolation functions ($\phi_i(\eta)$) that relate the displacement at any point along the beam element ($d_n(\eta)$) to the nodal displacements (d_n^A, θ_n^A, d_n^E, and θ_n^E). Hence the normal displacement at point B is given by

$$d_n^B(\eta) = \phi_1(\eta)d_n^A + \phi_2(\eta)\theta_n^A + \phi_3(\eta)d_n^E + \phi_4(\eta)\theta_n^E, \tag{6}$$

where d_n^B is the displacement of point B and η is the dimensionless distance of point B measured from node A ($\eta = b/L_e$). The maximum penetration distance (δ_B) is defined by the distance between point B and the support plane:

$$\delta_B = d_n^B - C_r, \tag{7}$$

where C_r is the radial clearance. The impact force can be calculated by

$$\begin{aligned}
\vec{F}_{\text{imp}} &= \vec{F}_{\text{spr}} + \vec{F}_{\text{dmp}},\\
\vec{F}_{\text{spr}} &= (K_{\text{spr}}\delta_B)\cdot\hat{u}_{smn},\\
\vec{F}_{\text{dmp}} &= -\text{sign}(\dot{\delta}_B)(1.5\alpha|K_{\text{spr}}\delta_B|)\cdot\hat{u}_{smn},
\end{aligned} \tag{8}$$

where $\vec{F}_{\text{spr}}$ is the spring force component resulting from considering a concentrated spring at point B. $\vec{F}_{\text{dmp}}$ accounts for the energy loss during an impact and α is an impact damping parameter related to the coefficient of the restitution as formulated by Hunt and Crossley (1975). The impact force can be decomposed into components in tube local the normal and axial directions:

$$\begin{aligned}
\vec{F}_{in} &= \vec{F}_{\text{imp}}\cdot\hat{u}_{tn},\\
\vec{F}_{ia} &= \vec{F}_{\text{imp}}\cdot\hat{u}_{ta}.
\end{aligned} \tag{9}$$

The frictional force acts in the plane containing the tube tangential velocity and the axial unit vectors. In order to calculate the frictional force, it is necessary to calculate the tube tangential velocity in the friction plane. The resultant tangential velocity, $\vec{V}_{rt}^{B}$, in the friction plane is calculated by the vectorial sum of the tube velocity components in the direction of $\hat{u}_{ta}$ and $\hat{u}_{tt}$. It must be noted that the velocity of point B has to be obtained by interpolating the velocity with respect to the nodal velocities. Three friction models are incorporated in this analysis: the velocity-limited friction model (VLFM), the spring damper friction model (SDFM), and the force balance friction model (FBFM). A description of these models can be found in the work of Antunes et al. (1992), Tan and Rogers (1996), and Hassan et al. (2003). For the sake of completeness, a brief review of these models is given below.

The "VLFM" was employed previously in loosely supported tube simulations (Rogers and Pick, 1977; Yetisir and Weaver, 1986; Fisher et al., 1991). In this model, a limiting velocity (V_0) is used to overcome the difficulties associated with the discontinuity of the classical Coulomb friction model. Depending on the value of the sliding velocity (V_t), the friction force F_f is either an arbitrary function of the velocity (a linear function is used in the above studies) or equal to the dynamic friction capacity, μF_{in}

$$|F_f| = \mu F_{in} \quad \text{if } |V_t| > V_o, \tag{10}$$

$$|F_f| = \frac{|V_t|}{V_o}\mu F_{in} \quad \text{if } |V_t| \leqslant V_o, \tag{11}$$

where μ is the kinetic coefficient of friction and F_{in} is the normal force.

Antunes et al. (1992) developed a SDFM, in which the sticking force is obtained by introducing an adherence stiffness and an adherence damper:

$$|F_f| = \mu F_{in} \quad \text{sliding}, \tag{12}$$

$$|F_f| = K_a(d_c - d_o) + C_a V_t, \tag{13}$$

where K_a and C_a are the adherence stiffness and damping, respectively, and d_c and d_o are the current and zero-velocity tangential displacements, respectively. Sticking is detected by a negative dot product of the present tangential velocity vector with its value at the previous time step.

In the FBFM, sticking is tested when the absolute velocity is less than a small limiting velocity (V_o). Friction force during sticking is calculated such that it balances the net force (Tan and Rogers, 1996):

$$F_f = Ku - F_e, \tag{14}$$

where Ku symbolically represents the internal tangential forces at the point of contact and F_e is the external forces. In order for sticking to occur in FBFM (and SDFM), F_f must satisfy the inequality

$$|F_f| < \mu_s F_{in}. \tag{15}$$

The user must specify a value for the static friction coefficient, μ_s.

Under the conditions of a small preload and no substantial initial eccentricity, a relatively simple friction model, the VLFM, was shown to give a good prediction of tube response, impact force and contact ratio as well as a conservative estimate of the work rate. However, sticking, which tends to prevent wear, is not well addressed in this model. The SDFM or the FBFM would be required if an initial contact or a significant preload were considered. A detailed comparison of the three methods in terms of accuracy and efficiency is presented in Hassan et al. (2003) and Hassan and Rogers (2004). In this work the FBFM will be utilized.

Using any one of the above-mentioned friction models, resultant frictional forces and moments are calculated, then translated to the tube local coordinates as follows:

$$\begin{aligned} F_{fa} &= \overrightarrow{F}_f \cdot \widehat{u}_{ta}, \quad M_{fa} = \overrightarrow{M}_f \cdot \widehat{u}_{ta}, \\ F_{ft} &= \overrightarrow{F}_f \cdot \widehat{u}_{tt}, \quad M_{ft} = \overrightarrow{M}_f \cdot \widehat{u}_{tt}. \end{aligned} \tag{16}$$

Now, the total contact forces in the local tube directions are:

$$\begin{aligned} F_{ca} &= F_{ia} + F_{fa}, \quad M_{ca} = M_{fa}, \\ F_{cn} &= F_{in}, \quad M_{cn} = 0, \\ F_{ct} &= F_{ft}, \quad M_{ct} = M_{ft}. \end{aligned} \tag{17}$$

The above expressions define the components of the contact forces at impact point B. However, in the finite element solution to structural vibrations, loads are applied at the nodes. Therefore, the impact and friction forces have to be expressed as concentrated loads and moments applied at the nodes. These nodal forces must be equivalent to these forces, in a virtual work sense. In other words, the work done by the impact forces is equal to the work done by the equivalent concentrated forces on the nodes. The work done by the impact and frictional forces is

$$W = F_{ca} d_a^B(\eta) + F_{cn} d_n^B(\eta) + F_{ct} d_t^B(\eta) + M_{ca} \theta_a^B(\eta) + M_{cn} \theta_n^B(\eta) + M_{ct} \theta_t^B(\eta). \tag{18}$$

The displacement components of this point are interpolated using the beam displacement functions. Hence, the consistent load vector equivalent to the impact and frictional forces is expressed by

$$\{P\} = \begin{Bmatrix} F_{ca}\psi_1(\eta) \\ F_{cn}\phi_1(\eta) + M_{ct}\sigma_1(\eta) \\ F_{ct}\gamma_1(\eta) \\ M_{ca}\lambda_1(\eta) \\ F_{ct}\gamma_2(\eta) \\ F_{cn}\phi_2(\eta) + M_{ct}\sigma_2(\eta) \\ F_{ca}\psi_2(\eta) \\ F_{cn}\phi_2(\eta) + M_{ct}\sigma_2(\eta) \\ F_{ct}\gamma_3(\eta) \\ M_{ca}\lambda_2(\eta) \\ F_{ct}\gamma_4(\eta) \\ F_{cn}\phi_4(\eta) + M_{ct}\sigma_4(\eta) \end{Bmatrix}, \tag{19}$$

where ψ_i, γ_i, λ_i, and σ_i are the beam interpolation function for the axial displacement, the tangential displacement, the axial rotation, and the tangential rotation, respectively. Now the global components of the load vector at nodes A and E are obtained by multiplying each force component with its respective unit vector.

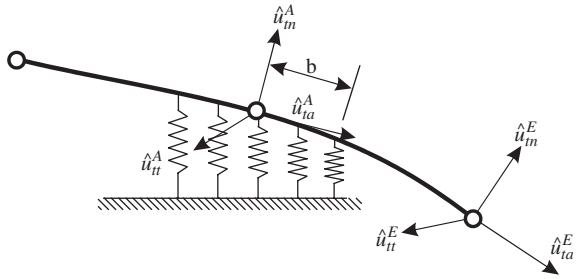

Fig. 5. The segment contact model.

2.2. Segment contact model

Segment contact occurs when the displacements of the PCN and/or PCN/NCN pair exceed the support gap. In both cases, the dimensionless overlap segment must be calculated. The dimensionless overlap segment is defined as the ratio of the contact segment length to the element length. Contact forces can be calculated by considering a distributed stiffness along the contact segment (b) as shown in Fig. 5. The strain energy of the deformed distributed stiffness is given by

$$U_g = \frac{K_g L_e}{2} \int (d_n(\xi) - C_r)^2 \, \mathrm{d}\xi, \tag{20}$$

where K_g is the gap stiffness, which is assumed to be constant and distributed over the overlap segment ($\eta = b/L_e$). The displacement $d_n(\xi)$ is interpolated using the beam displacement shape functions. Now integrating Eq. (20) yields

$$U_g = \frac{K_g L_e}{2} \begin{pmatrix} (d_n^A)^2 H_1 + L_e d_n^A \theta_t^A H_2 + d_n^A d_n^E H_3 + L_e d_n^A \theta_t^E H_4 \\ + d_n^A C_r H_5 + L_e^2 (\theta_t^A)^2 H_6 + L_e \theta_t^A d_n^E H_7 + L_e^2 \theta_t^A \theta_t^E H_8 \\ + L_e \theta_t^A C_r H_9 + (d_n^E)^2 H_{10} + L_e d_n^E \theta_t^E H_{11} + d_n^E C_r H_{12} \\ + L_e^2 (\theta_t^E)^2 H_{13} + L_e \theta_t^E C_r H_{14} + C_r^2 H_{13} \end{pmatrix}, \tag{21}$$

where H_1–H_{45} are polynomials of the dimensionless contact segment (η); see Appendix A. Now the nodal forces can be obtained by differentiating the strain energy expression with respect to the nodal degrees of freedom:

$$\{P_{\mathrm{spr}}\} = \begin{Bmatrix} F_n^A \\ M_t^A \\ F_n^E \\ M_t^E \end{Bmatrix} = \frac{K_g L_e}{2} \begin{bmatrix} 2H_1 & L_e H_2 & H_3 & L_e H_4 & H_5 \\ L_e H_2 & L_e^2 H_6 & L_e H_7 & L_e^2 H_8 & L_e H_9 \\ H_3 & L_e H_7 & 2H_{10} & L_e H_{11} & H_{12} \\ L_e H_4 & L_e^2 H_8 & L_e H_{11} & 2L_e^2 H_{13} & L_e H_{14} \end{bmatrix} \begin{Bmatrix} d_n^A \\ \theta_n^A \\ d_n^E \\ \theta_n^E \end{Bmatrix}. \tag{22}$$

The consistent load vector representing the friction force due to the relative motion between the tube and its support is obtained by considering the dissipated energy. The work done by the sliding friction forces in the axial direction is expressed as

$$W_{fa} = -\mu_d (\hat{u}_{tr} \cdot \hat{u}_{ta}) K_g L_e \int (d_n(\xi) - C_r) d_a(\xi) \, \mathrm{d}\xi, \tag{23}$$

where μ_d and $\hat{u}_{ta}$ are the dynamic friction coefficient and the resultant velocity vector (projected on the friction plane). By carrying out the integration of Eq. (23) and rearranging the resultant equation in matrix form, we have

$$W_{fa} = -\mu_d (\hat{u}_{tr} \cdot \hat{u}_{ta}) K_g L_e \begin{Bmatrix} d_a^A & d_a^A \end{Bmatrix} \begin{bmatrix} H_{11} & H_{12} & H_{13} & H_{14} & H_{15} \\ H_{21} & H_{22} & H_{23} & H_{24} & H_{25} \end{bmatrix} \begin{Bmatrix} d_n^A \\ L_e \theta_t^A \\ d_n^E \\ L_e \theta_t^E \\ C_r \end{Bmatrix}. \tag{24}$$

Hence the consistent load vector due to the axial component of the friction forces is

$$\{P_{fa}\} = -\mu_d(\widehat{u}_{tr}\cdot\widehat{u}_{ta})K_g L_e \begin{bmatrix} H_{11} & H_{12} & H_{13} & H_{14} & H_{15} \\ H_{21} & H_{22} & H_{23} & H_{24} & H_{25} \end{bmatrix} \begin{Bmatrix} d_n^A \\ L_e\theta_t^A \\ d_n^E \\ L_e\theta_t^E \\ C_r \end{Bmatrix}, \tag{25}$$

where H_{11}–H_{25} are polynomials of the dimensionless contact segment (η); see Appendix A. According to the FBFM the sticking condition is checked using inequality (15). In case of sticking, the adherence force is calculated based on net force as follows:

$$\{P_{fa}\} = [H]\{\{P_{ia}\} - \{P_{ea}\}\}, \tag{26}$$

where $\{P_{ia}\}$ and $\{P_{ea}\}$ are the internal and external load vectors in the axial direction. Similarly, the consistent load vector representing the sliding tangential friction force is given by

$$\{P_{ft}\} = -\mu_d(\widehat{u}_{tr}\cdot\widehat{u}_{tt})K_g L_e \begin{bmatrix} H_{11} & H_{12} & H_{13} & H_{14} & H_{15} \\ H_{21} & H_{22} & H_{23} & H_{24} & H_{25} \\ H_{31} & H_{32} & H_{33} & H_{34} & H_{35} \\ H_{41} & H_{42} & H_{43} & H_{44} & H_{45} \end{bmatrix} \begin{Bmatrix} d_n^A \\ L_e\theta_t^A \\ d_n^E \\ L_e\theta_t^E \\ C_r \end{Bmatrix}; \tag{27}$$

the polynomials H_{11}–H_{45} are also listed in Appendix A. In case of sticking, the adherence force is calculated as follows:

$$\{P_{ft}\} = [H]\{\{P_{it}\} - \{P_{et}\}\}, \tag{28}$$

where $\{P_{it}\}$ and $\{P_{et}\}$ are the internal and external load vectors in the tangential direction.

2.3. Finite element implementation

To calculate the time history of the tube response, a pseudo-force algorithm was used. In this procedure, impact forces were assumed to be known and the corresponding response was computed using the standard finite element solution of the beam equation:

$$[M]\{\ddot{d}\} + [C]\{\dot{d}\} + [K]\{d\} = \{F_e(t)\} + \{F_{\text{imp}}(d,\dot{d})\}. \tag{29}$$

The motion of the tube is described as a linear combination of the unconstrained modes. This permits the use of modal superposition to solve the system response, thereby saving considerable computational effort. The response converges rapidly to the correct solution as the number of modes used in the analysis increases. Typically, less than 10–20 modes in each direction are sufficient to achieve a reasonable representation of the constrained tube motion and the contact forces. Tube response is obtained by integrating the modal projection of Eq. (29) disregarding the tube/support contact. The Newmark (average acceleration) scheme is used for the integration of the nonlinear equations of motion. This implicit scheme is unconditionally stable. Based on the tube response obtained, clearance, type of support, and impact forces are then calculated. These forces include both the edge contact and the segment components from both sides of the PCN (right- and left-hand side elements). This process is repeated until convergence is attained in the impact forces. Convergence is measured by computing the Euclidean error norms of the impact forces of the previous iteration ($^{j-1}f_{in}$) with the current iteration impact force ($^{j}f_{in}$). Convergence is achieved when the relative error is less than a prescribed tolerance (ε_F).

$$\frac{\left[\sum_{i=1}^{N_{\text{sup}}} |{}^{j}f_{in_i} - {}^{j-1}f_{in_i}|^2\right]^{1/2}}{\left[\sum_{i=1}^{N_{\text{sup}}{}^{j}} ({}^{j}f_{in_i})^2\right]^{1/2}} \leqslant \varepsilon_F.$$

The authors' experience has shown that generally convergence is attained within 4–5 iterations if the integration time step is less than one-tenth the period of the highest mode included in the modal superposition. The aforementioned model was implemented in INDAP, an in-house finite element code (Dokainish, 1988) and was verified against several documented examples (Hassan et al., 2002).

3. Numerical simulations

Dimensionless parameters developed by Hassan et al. (2002) are reviewed briefly and will be used to present the current results. The radial tube/support clearance, C_r, is normalized by the r.m.s. resultant tube response with its support inactive response (d_{rsi}); d_{rsi} is the tube response at the support location obtained by applying the same excitation on the linear unconstrained system. Thus, the dimensionless clearance is C_r/d_{rsi}. The r.m.s. impact force (F_{imp}) is normalized by the total r.m.s. turbulence force. The total r.m.s. turbulence force is the product of the distributed turbulence force per unit length (F_{tur}) and the tube length, L. Thus, the dimensionless force is $F_{\text{imp}}/(F_{\text{tur}}L)$. The fluid excitation is expressed in terms of the reduced flow velocity, $U_R = U/fD$, where U is the mean flow velocity normal to the tube, f is the tube's natural frequency and D is the tube diameter. Normal work rate (W_N) is normalized by the input power induced by turbulence (W_{tur}). The total power absorbed by a tube of length (L) and mass per unit length (m) was expressed by Yetisir et al. (1998):

$$W_{\text{tur}} = \sum \frac{S_{FF}(f_i)J_i^2 L}{2m}, \tag{30}$$

where $S_{FF}(f_i)$ and J_i^2 are the PSD of the local force per unit length in the ith mode and the joint acceptance, respectively. Thus, the dimensionless normal work rate is W_N/W_{tur}. The lift (d_y) and drag (d_z) displacements of a point at a distance (x) from the fixed end are normalized, respectively by the r.m.s. lift (d_{ysi}) and drag (d_{zsi}) response of the unconstrained configuration (tube with support inactive), respectively. Finally, support width is normalized by the tube diameter, w/D.

3.1. Cantilever tube

The enhanced tube/support interaction model is used to investigate the effect of the support width on the tube dynamics. A cantilever tube of 617 mm length, 15.88 mm outer diameter, and 0.8 mm wall thickness, was utilised in these simulations. The equivalent mass per unit length and elastic modulus are 0.32 kg/m and 106 GPa, respectively. Simulations were carried out using 24 flexural modes each having 1% damping. The tube was loosely supported at the free end (Fig. 6) by rhomboid flat-bar (lattice bars) supports. The support is placed at the 30th node (at 0.021 m from the tip of the tube). Four support width values are used: 10, 15, 20, and 25 mm, which when normalized by the tube diameter, give dimensionless support widths of 0.63, 0.94, 1.26, and 1.57, respectively. The tube is subjected to a flow of air at a density of 1.18 kg/m^3 at a velocity of 8 m/s. The fluid excitation due to turbulence is modelled as randomly distributed forces. The bounding power spectral density (PSD) measured by Oengören and Ziada (1998) for a tube array of pitch-to-diameter ratio (P/D) of 1.61 was utilized in this work to generate the time-domain fluid forces. However, the results are independent of the choice of bounding spectra when presented in the dimensionless form (Hassan et al., 2002). The PSD curve of turbulence excitation is obtained depending on the flow velocity, the tube's diameter and the array geometry. This PSD curve is then transformed into a force–time record using an inverse Fourier transform algorithm with random phases. Two different force versus time records were used representing the fluid excitation in the lift and the drag directions. The lift force record contains only a fluctuating force component with a zero mean. On the other hand, the drag force record consists of the fluctuating force component superimposed on a static component representing the steady drag forces. Fluid forces are assumed to be fully correlated along the span of the tube; however, the two force components, drag and lift, are fully uncorrelated. A point support stiffness of 10^5–10^7 N/m has been reported in the literature (Rogers and Pick, 1977; Axisa et al., 1988). However, these papers demonstrated that the impact forces are rather insensitive to the support stiffness in this range.

The value of the distributed contact stiffness is also needed for the model developed here. Therefore, a detailed finite element modelling of the tube/support contact was conducted. The distributed contact stiffness was calculated by dividing the applied distributed load by the resulting average tube deformation. In addition several simulations were

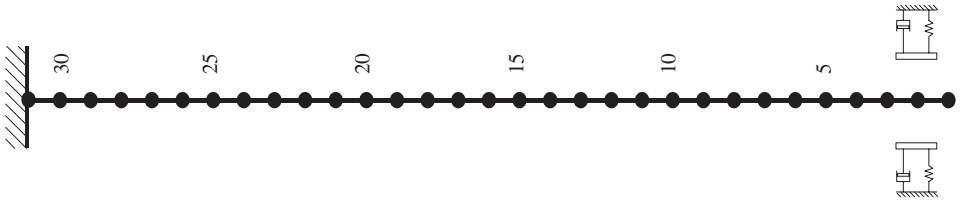

Fig. 6. Tube/support finite element model.

conducted to study the effect of changing the distributed stiffness on the tube dynamics. Similar to the conclusion of Rogers and Pick (1977) and Axisa et al. (1988), the study showed very weak dependency of results on the choice of the distributed stiffness in the range of 1×10^8–5×10^8 N/m^2 (when the stiffness is increased by 500%, the r.m.s. impact force increases by a mere 3.7%, while the contact ratio decreases by 2%). A single coefficient of friction value of 0.1. This is a lower value than that what is expected [a value of 0.36 was reported by Haslinger and Steininger (1995)] and previous works (de Langre et al., 1992; Hassan et al., 2003) have shown that friction coefficient has little effect on the impact force, lift response, and contact ratio. However, this value of the friction coefficient represents a reasonable lower bound and would give a conservative prediction of the wear rate.

For each case study, 5 s of response time history were computed. The tube/support interaction parameters were averaged over the simulation time record, excluding the initial transient period. Using the enhanced tube/support model, both the segment and the edge contact were identified. The tube support interaction parameters, including the r.m.s. impact forces, the contact ratio and the normal work rate, were calculated for both the segment and the edge contact situations.

Simulation results showed that using the new model, the support acts more like a clamped end condition in which the clearance is small. This was confirmed by the appearance of a peak at a frequency slightly less than the fixed–fixed frequency in the power spectral density curves of the response for small clearances. As the clearance increases, the support behaves more like a pinned support and the natural frequency shifts downward.

The r.m.s. of the impact force components (segment and edge contact) for various support width values are shown in Fig. 7. The segment contact force component is shown in Fig. 7(a), in which similar behaviour can be observed for all support width values. As the clearance increases from very small values, the r.m.s. impact force decreases approximately in a linear fashion, followed by a sharp decrease at dimensionless clearances around 0.2. Up to this point, the r.m.s. impact force results approach those obtained by the SPCM when the support width approaches zero. As the clearance increases further and/or the support width decreases, the segment contact force component decreases to zero since the contact tends to be a point-like contact.

Fig. 7(b) depicts the dimensionless r.m.s. impact force resulting from the tube/support edge contact for various support width values. For any finite support width, the dimensionless point impact force component is zero when the dimensionless clearance is zero. Increasing the dimensionless clearance increases the point impact force. This behaviour is maintained up to a dimensionless clearance of about 0.2 or larger, depending on the support width, beyond which the impact force starts to decrease linearly. At this point the results converge to a single curve and become independent of the support width. This is because enlarging the dimensionless clearance provides a favourable condition for the tube to impact with the support at its edge. On the other hand, at a small clearance the contact configuration is mainly of the segmental type. This is because there is a better alignment of the tube with the support, and hence a segmental contact is promoted. Clearly, the dominant contact mode is strongly dependent on the support width and clearance. It must be noted that the two types of contact may occur simultaneously or individually, but the frequency of their occurrence depends on the clearance and support width. It is worth also noting that after adding "segment impact" (Fig. 7(a)) and the "point impact" (Fig. 7(b)) results, the total value is close to the results from the basic SPCM model.

Fig. 8(a) shows the contact ratio due to segment contact as a function of the dimensionless clearance. As expected, for all support width values, the tube has a 100% segment contact with the support at very small clearances. For a small support width, the tube continues to maintain a high segment-type of contact with the support for a range of dimensionless clearances. The range of dimensionless clearances permitting continuous segment contact decreases as the support width increases. Similar to the SPCM results, a decrease in the contact ratio is observed when the clearance increases beyond a certain value. It then levels off asymptotically to zero as edge contact is established. For a given dimensionless clearance, the segment contact ratio increases as the support width decreases. Hence, the larger the support width, the lower the dimensionless clearance at which the tube does not maintain a segment contact with the support. In addition the segment contact solution approaches the solution obtained using the SPCM when the support width approaches zero.

It is worth noting here that while the segmental components of the r.m.s. impact force and the contact ratio approach those of the SPCM when the support width approaches zero, the same should not be expected for the edge contact. This is because the edge contact solution represents a situation in which the tube contacts the support at its edge, a situation not modelled in the SPCM. In this situation the PCN lies within the support space (no overlap), which is considered a no-contact condition using the SPCM.

The contact ratio of the tube with the support edge is depicted in Fig. 8(b) for various support width values. At small clearances, segment type of contact is promoted and the edge contact ratio is very low. As the clearance is increased, the edge contact ratio increases dramatically, this effect occurring at smaller clearances for larger support widths. At a dimensionless clearance of about 0.2, or larger for smaller support widths, the edge contact ratio decreases and becomes independent of support width for increasing clearances.

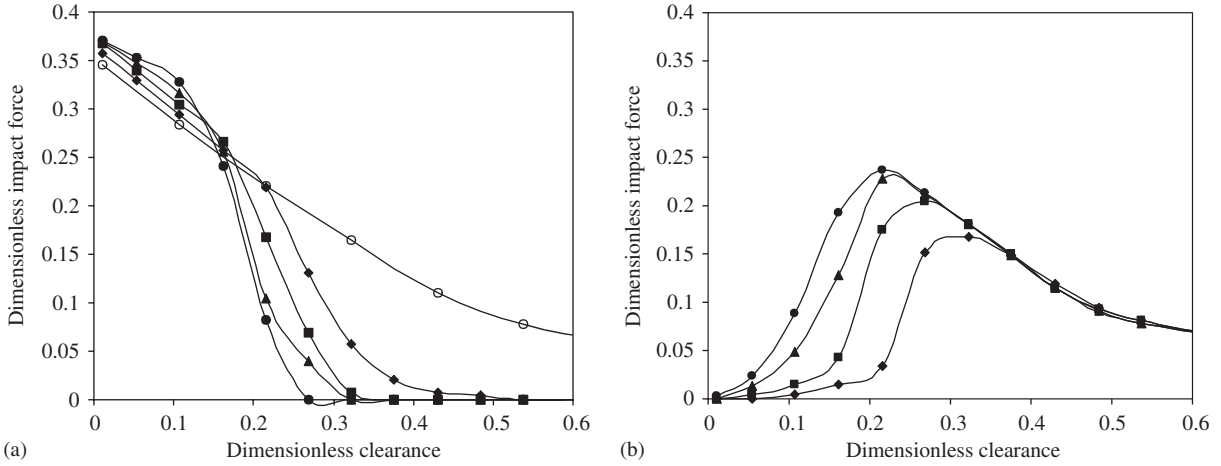

Fig. 7. Effect of the support width on the r.m.s. impact force: ◆, $w/D = 0.63$; ■, $w/D = 0.94$; ▲, $w/D = 1.26$; ●, $w/D = 1.56$; ◯, SPCM: (a) segment impact force and (b) point impact force.

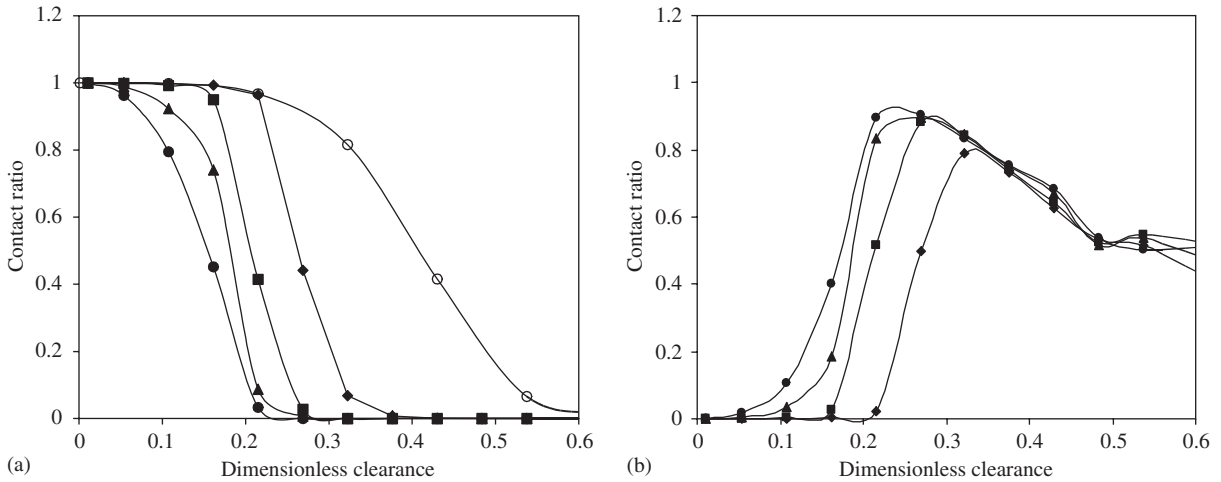

Fig. 8. Effect of the support width on the contact ratio: ◆, $w/D = 0.63$; ■, $w/D = 0.94$; ▲, $w/D = 1.26$; ●, $w/D = 1.56$; ◯, SPCM: (a) segment contact and (b) edge contact.

The dimensionless work rate for the segment contact forces is shown in Fig. 9(a). In the case of a tube with a dimensionless support width of 0.63, the work rate decreases nearly linearly up to a dimensionless clearance of approximately 0.2. Then it decreases asymptotically to zero. For a higher support width, the work rate increases to a maximum value then decreases for a further increase in support clearance. Larger support widths exhibit higher work rate peaks at lower clearances. The normal work rate resulting from edge contact is shown in Fig. 9(b). At small clearances the contact ratio is zero and therefore the work rate is zero. As edge contact is developed for increasing clearances, the work rate increases to a maximum depending on support width, the smaller the support width, the higher the dimensionless clearance at which the work rate peak occurs. Note the different work rate scales in Fig. 9(a) and (b). The normal work rate curves are lower than those of segment contact for all support width values.

3.2. Two-span tube

The relative importance of segment or edge contact will depend on the slope of a tube in a normal mode at an inactive support. To study this effect, a two-span tube configuration was examined. This configuration consists of a 1.19 m long tube fixed at both ends and loosely supported by a pair of flat bars at the middle. The tube material and cross-section

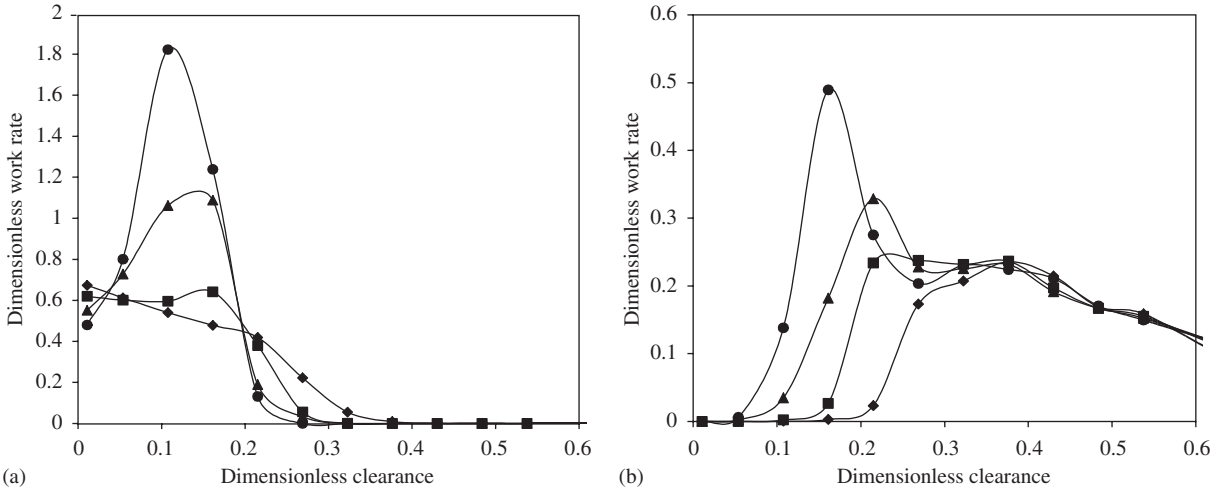

Fig. 9. Effect of the support width on the normal work rate: ◆, $w/D = 0.63$; ■, $w/D = 0.94$; ▲, $w/D = 1.26$; ●, $w/D = 1.56$: (a) segment contact and (b) edge contact.

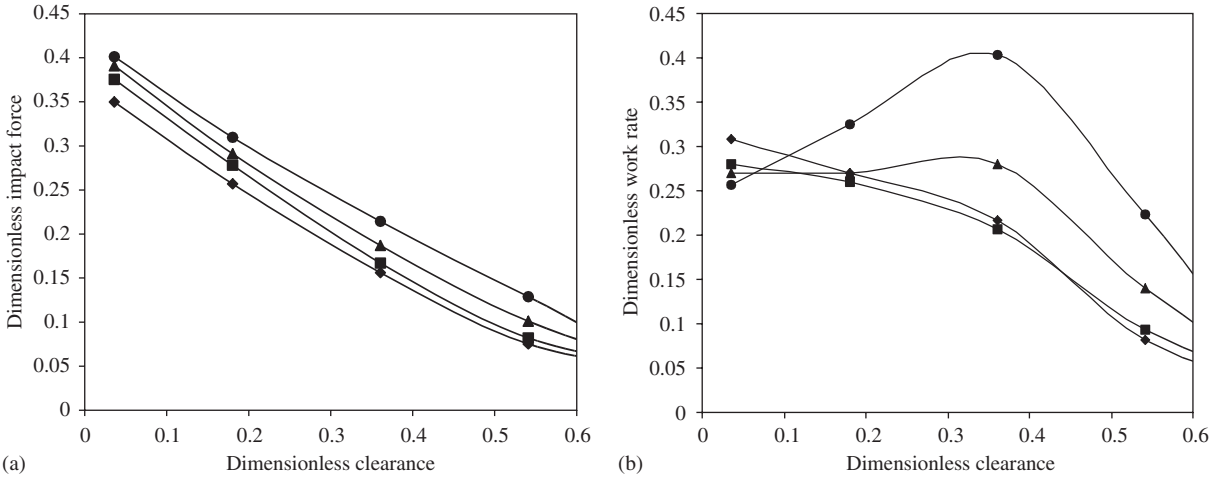

Fig. 10. Two-span tube results: ◆, $w/D = 0.63$; ■, $w/D = 0.94$; ▲, $w/D = 1.26$; ●, $w/D = 1.56$: (a) r.m.s. impact force and (b) normal work rate.

properties are identical to those of the cantilever tube model used in Section 3.2. The tube was excited by turbulence forces which are distributed along the entire length of the tube as in the previous case. The first unconstrained mode has an anti-node with a zero-slope at the support location. This profile of the unconstrained mode, along with the spatial distribution of the turbulence forces, provides a favourable condition for segmental contact rather than edge contact. Fig. 10(a) depicts the effect of the dimensionless clearance on the dimensionless r.m.s. impact force. The computation showed that the tube/support contact was due only to segmental contact and no edge contact was observed. Thus, the r.m.s. impact force behaviour is similar to that for the segmental component of the SPCM as seen in Fig. 7(a). Interestingly, the r.m.s. impact force increases with increasing support width.

The dimensionless work rate for the segment contact forces is shown in Fig. 10(b). For small dimensionless clearances (<0.1), the dimensionless work rate decreases as the support width increases while the opposite is true for large clearances. For intermediate clearances (0.1–0.5), the work rate actually rises to a peak for dimensionless support widths greater than about 1.0, the peak value increasing with support width. This may be attributed to midspan tube curvature relative to support width at larger clearances.

4. Tube wear

The ultimate goal of fretting wear analysis is to estimate the loss in tube wall thickness. This is accomplished by utilizing the normal work rate. The normal work rate, which is defined as the integral of the normal contact force and the sliding distance per unit time, is usually used to calculate the fretting wear volume rate

$$\dot{V} = C_w \dot{W}, \tag{31}$$

where C_w is the wear coefficient obtained experimentally. The literature suggests that the wear coefficient for continuous sliding is larger than the wear coefficient for fretting (Connors, 1981). Using this equation, the volumetric loss can be calculated. The cumulative tube wall loss can be expressed as follows:

$$h(t) = \int \dot{h}(t)\,\mathrm{d}t, \tag{32}$$

where $\dot{h}$ is the rate of the wall thickness loss which is a function of the volume wear rate. The cumulative depth of wear must be calculated incrementally. This is because, as the tube thickness decreases due to wear, the tube-to-support clearance increases. This in turn changes the nonlinear dynamics of the tube. As a result, the normal work rate changes with time as the tube wall wears out. The relationship between the normal work rate and the support clearance can be obtained using the nonlinear simulation carried out in Section 3. The incremental procedure starts by considering an initial radial tube-to-support clearance $C_r(t_o)$ at time t_o. After a time increment of t, a volume V is removed from the tube. This volume rate can be calculated using Eq. (31). The tube wear depth associated with this wear volume can be determined by defining the geometry of the wear scar. The geometrical relationship between the wear volume and the wear depth of a tube contacting a flat-bar support is used to calculate the wear depth, h. For simplicity, it is assumed that only the tube wears, while the support (flat bar) maintains its original shape, and the scar is uniform along the support width. In terms of tube damage these are conservative assumptions.

Now, the current radial tube-to-support clearance must be updated to reflect the loss of tube thickness at the support location as follows:

$$C_r(t) = C_r(t_o) + h(t). \tag{33}$$

This new support clearance value will result in a change in the current normal work rate which can be obtained from Fig. 10(b). These calculations continue until the wall thickness reaches a target value. For the calculations presented in this Section, C_w will be assumed to be equal to $40 \times 10^{-15}\,\mathrm{Pa}^{-1}$ (Connors, 1981). The same wear coefficient will be used for continuous sliding and for intermittent impact. The purpose of these calculations is to illustrate the effect of the support width on tube wear rather than to estimate heat exchanger life. Therefore, the simplified example provided herein represents a portion of the overall evaluation that is required. Fig. 11 depicts the calculated dimensionless depth of wear ($h(t)/d_{rsi}$) for different support width values. These curves were produced for the two-span tube configuration discussed in Section 3.2. The initial dimensionless clearance was 0.036 and is updated at a time increment of 10^5 s. The time was incremented until the dimensionless clearance reached a value of 0.36. The results show that the rate of tube wear depth decreases with time as wear volume is distributed over a larger area of the tube surface and that increasing the support width results in a lower depth of wear. This wear prediction behaviour agrees with the findings of Guérout and Fisher (1999) and Langford and Connors (1991).

These results demonstrate the importance of including a finite contact area in computing wear. The examples considered in Sections 3.1 and 3.2 above showed that increasing the support width increases the segmental r.m.s. impact force and the work rate. However, this segmental contact force is distributed over a larger area as the support width is increased and, therefore, the larger impact force may be less damaging in terms of wear. To investigate this possibility further, the r.m.s. segmental impact pressure (impact force per unit support width), P_{imp}, is computed using the instantaneous impact force, $F_{\mathrm{imp}}(t)$, and segmental contact length, $b(t)$, by

$$P_{\mathrm{imp}} = \left\{ \lim_{(t_2-t_1)\to\infty} \left[\frac{1}{t_2 - t_1} \int_{t_1}^{t_2} \left(\frac{F_{\mathrm{imp}}(t)}{b(t)} \right)^2 \mathrm{d}t \right] \right\}^{1/2}. \tag{34}$$

This contact pressure is normalised using the applied turbulence force per unit of tube length, P_{tur}, to give the effective dimensionless contact pressure, P:

$$P = \frac{P_{\mathrm{imp}}}{P_{\mathrm{tur}}}. \tag{35}$$

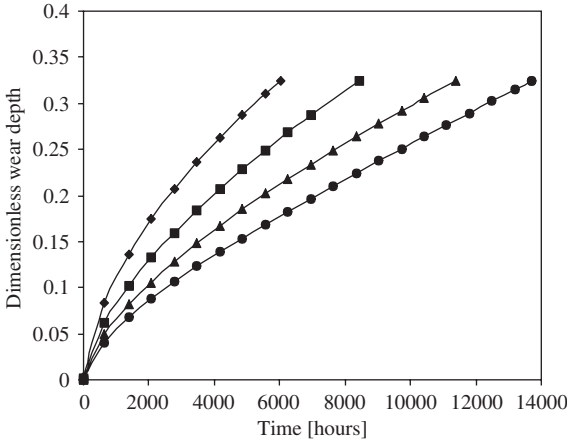

Fig. 11. Predicted dimensionless wear depth versus time: ◆, $w/D = 0.63$; ■, $w/D = 0.94$; ▲, $w/D = 1.26$ and ●, $w/D = 1.56$.

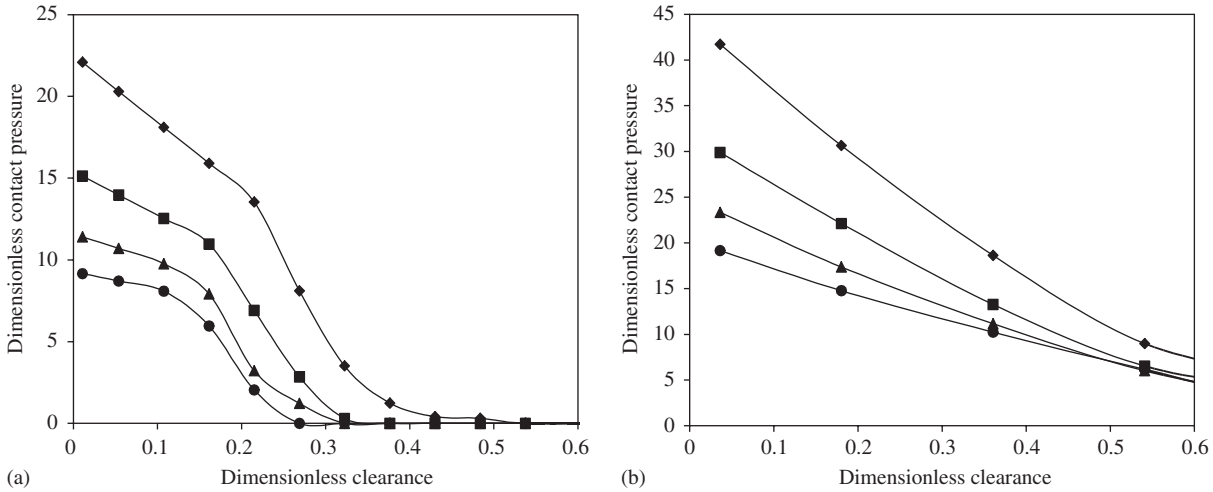

Fig. 12. The dimensionless contact pressure: ◆, $w/D = 0.63$; ■, $w/D = 0.94$; ▲, $w/D = 1.26$; ●, $w/D = 1.56$: (a) cantilever tube case and (b) two-span tube case.

P is plotted against dimensionless clearance for the cantilever tube of Section 3.1 and the two-span tube of Section 3.2 in Figs. 12(a) and 12(b), respectively. Four different support widths are considered in each case. It is apparent that the contact pressure decreases as the support width increases. Contact pressure can have a great effect on the work rate. Greater wear rates were observed for smaller areas of contact (Fisher et al., 1995). This effect was attributed to the differences in the contact pressure (Lim and Ashby, 1987). Simplifying the tube/support structure to a single-point contact seems to be a useful approximation when predicting the total r.m.s. impact force. However, since the details of the tube motion, contact force distribution and the contact type are very important in terms of contact pressure, using the single-point contact assumption may be an oversimplification when studying the effect of the support geometry on the wear rates.

5. Conclusions

A tube/support interaction model was developed to simulate the contact more realistically. In this model, the support width was taken into account when calculating the contact forces and the work rate. The tube/support contact was modelled by a distributed stiffness to account for the segment contact. The impact forces were distributed along

the contact segment using the beam displacement interpolation function. The equivalent nodal force vector was derived in a manner consistent with the finite element formulation. The model was also capable of expressing any inter-nodal point contact which may be encountered. Numerical simulations were carried out using the new model to examine the effect of the support width on the tube dynamics. The general conclusions drawn from this study are listed below.

(i) An advantage of modelling tube/support interaction with finite support width over the traditional point contact approach is that it more realistically accounts for the rotational stiffness of the support and its effects on the tube mode shape, frequency and tube/support contact area.
(ii) Tube/support impact is shown to be a combination of edge (point) and segmental (line) contact, the relative importance of each depending on the mode shape and tube-to-support clearance.
(iii) Smaller tube/support clearances tend to produce segmental contact and therefore larger contact areas as well as increased support stiffness against tube rotation. These effects are enhanced by increased support width.
(iv) Decreased clearance and increased support width produce higher impact forces and work rates but the wear rate is reduced because of the increased contact area (reduced contact pressure).

Acknowledgments

The authors thankfully acknowledge the financial support provided by the Natural Sciences and Engineering Research Council of Canada.

Appendix A. Polynomials used in the analysis, in Section 2.2

H_1–H_{15} polynomials of the dimensionless contact used in Eq. (22).

$$H_1=\tfrac{4}{7}\eta^7-2\eta^6+\tfrac{9}{5}\eta^5+\eta^4-2\eta^3+\eta,\quad H_2=\tfrac{4}{7}\eta^7-\tfrac{7}{3}\eta^6+\tfrac{16}{5}\eta^5-\eta^4-\tfrac{4}{3}\eta^3+\eta^2,$$
$$H_3=-\tfrac{8}{7}\eta^7+4\eta^6-\tfrac{18}{5}\eta^5-\eta^4+2\eta^3,\quad H_4=\tfrac{4}{7}\eta^7-\tfrac{5}{3}\eta^6+\tfrac{6}{5}\eta^5+\tfrac{1}{2}\eta^4-\tfrac{2}{3}\eta^3,$$
$$H_5=-\eta^4+2\eta^3-2\eta,\quad H_6=\tfrac{1}{7}\eta^7-\tfrac{2}{3}\eta^6+\tfrac{6}{5}\eta^5-\eta^4+\tfrac{1}{3}\eta^3,$$
$$H_7=-\tfrac{4}{7}\eta^7+\tfrac{7}{3}\eta^6+\tfrac{16}{5}\eta^5+\tfrac{3}{2}\eta^4,\quad H_8=\tfrac{2}{7}\eta^7-\eta^6+\tfrac{6}{5}\eta^5-\eta^4,$$
$$H_9=-\tfrac{1}{2}\eta^4+\tfrac{4}{3}\eta^3-\eta^2,\quad H_{10}=\tfrac{4}{7}\eta^7-2\eta^6+\tfrac{9}{5}\eta^5,$$
$$H_{11}=-\tfrac{4}{7}\eta^7-\tfrac{5}{3}\eta^6-\tfrac{6}{5}\eta^5,\quad H_{12}=\eta^4-2\eta^3,$$
$$H_{13}=\tfrac{1}{7}\eta^7-\tfrac{1}{3}\eta^6+\tfrac{1}{5}\eta^5,\quad H_{14}=-\tfrac{1}{2}\eta^4+\tfrac{2}{3}\eta^6,\quad H_{15}=\eta.$$

H_{11}–H_{25} are polynomials of the dimensionless contact segment used in Eq. (25).

$$H_{11}=-\tfrac{2}{5}\eta^5=\tfrac{5}{4}\eta^4-\eta^3-\tfrac{1}{2}\eta^2+\eta,\quad H_{12}=-\tfrac{1}{5}\eta^5+\tfrac{3}{4}\eta^4-\eta^3+\tfrac{1}{2}\eta^2,$$
$$H_{13}=\tfrac{2}{5}\eta^5-\tfrac{5}{4}\eta^4+\eta^3,\quad H_{14}=-\tfrac{1}{5}\eta^5+\tfrac{1}{2}\eta^4-\tfrac{1}{3}\eta^3,$$
$$H_{15}=\tfrac{1}{2}\eta^2-\eta,\quad H_{21}=\tfrac{2}{5}\eta^5-\tfrac{3}{4}\eta^4+\tfrac{1}{2}\eta^2,$$
$$H_{22}=\tfrac{1}{5}\eta^5-\tfrac{1}{2}\eta^4+\tfrac{1}{3}\eta^3,\quad H_{23}=-\tfrac{2}{5}\eta^5-\tfrac{3}{4}\eta^4,$$
$$H_{24}=\tfrac{1}{5}\eta^5-\tfrac{1}{4}\eta^4,\quad H_{25}=-\tfrac{1}{5}\eta^2.$$

H_{11}–H_{45} are polynomials of the dimensionless contact segment used in Eq. (27).

$$H_{11}=\tfrac{4}{7}\eta^7-2\eta^6+\tfrac{9}{5}\eta^5+\eta^4-2\eta^3+\eta,\quad H_{12}=-\tfrac{4}{7}\eta^7-2\eta^6+\tfrac{9}{5}\eta^5-\tfrac{1}{2}\eta^4-\eta^3,$$
$$H_{13}=\tfrac{2}{7}\eta^7-\tfrac{7}{6}\eta^6+\tfrac{8}{5}\eta^5-\tfrac{1}{2}\eta^4-\tfrac{2}{3}\eta^3+\tfrac{1}{2}\eta^2,\quad H_{14}=\tfrac{2}{7}\eta^7-\tfrac{5}{6}\eta^6+\tfrac{3}{5}\eta^5+\tfrac{1}{4}\eta^4-\tfrac{1}{3}\eta^3,$$
$$H_{15}=-\tfrac{1}{2}\eta^4+\eta^3-\eta,\quad H_{21}=-\tfrac{2}{7}\eta^7+\tfrac{7}{6}\eta^6-\tfrac{8}{5}\eta^5-\tfrac{1}{2}\eta^4+\tfrac{2}{3}\eta^3-\tfrac{1}{2}\eta^2,$$
$$H_{22}=-\tfrac{1}{7}\eta^7+\tfrac{2}{3}\eta^6-\tfrac{6}{5}\eta^5+\eta^4-\tfrac{1}{2}\eta^3,\quad H_{23}=\tfrac{2}{7}\eta^7-\tfrac{7}{6}\eta^6+\tfrac{8}{5}\eta^5-\tfrac{3}{4}\eta^4,$$

$$H_{24} = -\tfrac{1}{7}\eta^7 + \tfrac{1}{2}\eta^6 - \tfrac{3}{5}\eta^2 + \tfrac{1}{4}\eta^4, \quad H_{25} = \tfrac{1}{4}\eta^4 - \tfrac{2}{3}\eta^3 + \tfrac{1}{2}\eta^2,$$
$$H_{31} = -\tfrac{4}{7}\eta^7 - 2\eta^6 - \tfrac{9}{5}\eta^5 - \tfrac{1}{2}\eta^4 + \eta, \quad H_{32} = -\tfrac{2}{7}\eta^7 + \tfrac{7}{6}\eta^6 - \tfrac{8}{5}\eta^5 + \tfrac{3}{4}\eta^4,$$
$$H_{33} = \tfrac{4}{7}\eta^7 - 2\eta^6 + \tfrac{9}{5}\eta^5, \quad H_{34} = -\tfrac{2}{7}\eta^7 + \tfrac{5}{6}\eta^6 - \tfrac{3}{5}\eta^5,$$
$$H_{35} = \tfrac{1}{2}\eta^4 - \eta^3, \quad H_{41} = -\tfrac{2}{7}\eta^7 - \tfrac{5}{6}\eta^6 - \tfrac{3}{5}\eta^5 - \tfrac{1}{4}\eta^4 - \tfrac{1}{3}\eta^3,$$
$$H_{42} = -\tfrac{1}{7}\eta^7 + \tfrac{1}{2}\eta^6 - \tfrac{3}{5}\eta^5 + \tfrac{1}{4}\eta^4, \quad H_{43} = -\tfrac{2}{7}\eta^7 - \tfrac{5}{6}\eta^6 + \tfrac{3}{5}\eta^5,$$
$$H_{44} = -\tfrac{1}{7}\eta^7 + \tfrac{1}{3}\eta^6 - \tfrac{1}{5}\eta^5, \quad H_{45} = \tfrac{1}{4}\eta^4 - \tfrac{1}{3}\eta^6.$$

References

Antunes, J., Axisa, F., Beaufils, B., Guilbaud, D., 1992. Coloumb friction modelling in numerical simulations of vibration and wear work rate of multispan tube bundles. Journal of Fluids and Structures 4, 287–304.

Axisa, F., Antunes, J., Villard, B., 1988. Overview of numerical methods for predicting flow-induced vibration. ASME Journal of Pressure Vessel Technology 110, 6–14.

Chen, S.S., 1991. A review of dynamic tube–support interaction in heat exchanger tubes. In: Proceedings of the International Conference on Flow Induced Vibrations. IMechE, Brighton, UK, pp. 111–120.

Connors, H., 1991. Flow-induced vibration and wear of steam generator tubes. Nuclear Technology 55, 311–331.

de Langre, E., Hadj-Sadok, C., Beaufils, B., 1992. Non-linear vibrations induced by fluidelastic forces in tube bundles. In: Proceedings of the Symposium on Flow-Induced Vibrations and Noise. ASME, Anaheim, pp. 107–134.

Dokainish, M., 1988. Incremental Nonlinear Dynamic Analysis Program: Theoretical Manual. McMaster University, Canada.

Fisher, N., Olesen, M., Rogers, R., Ko, P., 1989. Simulation of tube-to-support dynamic interaction in heat exchange equipment. ASME Journal of Pressure Vessel Technology 111, 378–384.

Fisher, N., Pettigrew, M., Rogers, R., 1991. Fretting wear damage prediction in the inlet region of nuclear steam generators. In: Proceedings of the Fifth International Conference on Flow Induced Vibrations.

Fisher, N.J., Chow, A.B., Weckwerth, M.K., 1995. Experimental fretting-wear studies of steam generator materials. ASME Journal of Pressure Vessel Technology 117, 312–319.

Guérout, F., Fisher, N., 1999. Steam generator fretting-wear damage: a summary of recent findings. ASME Journal of Pressure Vessel Technology 121, 210–304.

Haslinger, K., Steininger, D., 1995. Experimental characterization of sliding and impact friction coefficients between steam generator tubes and AVB supports. Journal of Sound and Vibration 181, 851–871.

Hassan, A., Rogers, R., 2004. Friction modelling of preloaded tube contact dynamics. In: de Langre, E., Axisa, F. (Eds.), The Eighth International Conference on Flow-Induced Vibration, Palaiseau, France, pp. 295–300.

Hassan, M., Weaver, D., Dokainish, M., 2002. A simulation of the turbulence response of heat exchanger tubes in lattice-bar supports. Journal of Fluids and Structures 16, 1145–1176.

Hassan, M.A., Weaver, D.S., Dokainish, M.A., 2003. The effects of support geometry on the turbulence response of loosely supported heat exchanger tubes. Journal of Fluids and Structures 18, 529–554.

Hunt, K.H., Crossley, F.R., 1975. Coefficient of restitution interpreted as damping in vibroimpac. Journal of Applied Mechanics 43, 440–445.

Kim, B., Pettigrew, M., Tromp, J., 1988. Vibrations damping of heat exchanger tubes in liquids: effects of support parameters. Journal of Fluids and Structures 2, 593–614.

Ko, P.L., 1985. Heat exchanger tube fretting wear: review and application to design. ASME Journal of Technology 107, 149–156.

Langford, P., Connors, H., 1991. Calculation of tube-AVB wear from U-bend shaker test data. In: Proceedings of the Fifth International Conference on Flow Induced Vibrations, pp. 45–55.

Lim, S.C., Ashby, M.F., 1987. Wear mechanism maps. Acta Metallurgica 35, 1–24.

Morandin, G., Sauvé, R., 1999. Formulation of an analog boundary element with application to process equipment tube supports. In: Flow-Induced Vibration, PVP-vol. 389. ASME, New York, pp. 245–253.

Oengören, A., Ziada, S., 1998. An in-depth study of vortex shedding, acoustic resonance and turbulent forces in normal triangle tube arrays. Journal of Fluids and Structures 12, 717–758.

Païdoussis, M., 1982. A review of flow-induced vibrations in reactors and reactor components. Nuclear Engineering and Design 74, 31–60.

Pettigrew, M.J., Taylor, C.E., 2003. Vibration analysis of steam generators and heat exchangers: an overview, Part 1: flow damping, fluidelastic instability. Journal of Fluids and Structures 18, 469–483.

Rogers, R., Pick, R., 1977. Factors associated with support plate forces due to heat exchanger tube vibratory contact. Nuclear Engineering and Design 44, 247–253.

Sauvé, R., Teper, W., 1987. Impact simulation of process equipment tubes and support plates—a numerical algorithm. ASME Journal of Pressure Vessel Technology 109, 70–79.

Tan, X., Rogers, R., 1996. Dynamic friction modelling in heat exchanger tube simulations. In: Pettigrew, M. (Ed.), Flow-Induced Vibrations, vol. 328. ASME, Montréal, pp. 347–358.

Weaver, D.S., Ziada, S., Au-Yang, M.K., Chen, S.S., Païdoussis, M.P., Pettigrew, M.J., 2000. Flow-induced vibrations in power and process plant components—progress and prospects. ASME Journal of Pressure Vessel Technology 122, 339–348.

Yetisir, M., Weaver, D., 1986. The dynamics of heat exchanged U-bend tubes with flat-bar supports. ASME Journal of Pressure Vessel Technology 108, 406–412.

Yetisir, M., McKerrow, E., Pettigrew, M.J., 1998. Fretting wear damage of heat exchanger tubes: a proposed damage criterion based on tube vibration response. ASME Journal of Pressure Vessel Technology 120, 297–305.